

# Thermodynamic Analysis of TiN Precipitation in SWRH92A High Carbon Tire Cord Steel Under the Influence of Solute Micro-segregations During Solidification



PENG WANG, CHENGZHI LI, LU WANG, JUHUA ZHANG, and ZHENGLIANG XUE

The precipitation of TiN inclusion during the solidification of SWRH92A high carbon tire cord steel has been thermodynamically calculated. The influence of solute micro-segregations calculated by Ohnaka and Clyne–Kurz models, respectively, on the thermodynamic parameters is considered. The TiN precipitation module is coupled with the Ti and N micro-segregations when the condition of TiN precipitation is satisfied. Furthermore, the TiN growth is predicted based on the thermodynamic calculation results. The results first show that the solute elements of molten steel segregate to different extents during solidification. The carbon concentration increases most significantly by about 1.8 wt pct due to its highest original content. By coupling TiN precipitation module with solute micro-segregation module, the segregated ratios of Ti and N decrease after the TiN inclusion starts precipitating. With cooling rate increasing from 0.17 to 1.67 K/s, TiN precipitation starts earlier, but the TiN particle size decreases from about 10 to about 3  $\mu\text{m}$ . The TiN inclusion sizes calculated in the Ohnaka and Clyne–Kurz model cases are close and well validated by the metallographic images of TiN inclusions and the statistical data of TiN particle size distribution in high carbon tire cord steels. This agreement encourages the proposed calculation method and provides guidance for the future thermodynamic studies of nonmetallic inclusions of steel.

<https://doi.org/10.1007/s11663-021-02166-x>

© The Minerals, Metals & Materials Society and ASM International 2021

## I. INTRODUCTION

THE non-oxide inclusions of steel products, such as nitride and sulfide inclusions, normally precipitate in the liquid–solid mushy zone during the solidification process due to the micro-segregations of solute elements. With the enrichment of these elements in the inter-dendrite liquid pool, the actual activity products of some non-oxide inclusions tend to be larger than their equilibrium activity products as the temperature decreases to certain values. As a result, the corresponding inclusions would begin to precipitate and then grow

up. Therefore, the non-oxide inclusions normally form under a non-isothermal, concentration-varying, and finite “time and space” condition. Once these inclusions precipitate in the steel products, they cannot be effectively removed.

Non-oxide inclusions are generally harmful to the quality of steel products. TiN, a typical nitride inclusion, is non-deformable and has extremely high strength.<sup>[1,2]</sup> The formation of TiN in tire cord steel, especially in hypereutectoid high carbon tire cord steel, would significantly increase the chances of filament break and delamination during the wire drawing process and deteriorate the fatigue properties of the final products. The specific hazards of TiN for tire cord steel have been illustrated in many studies.<sup>[3–6]</sup> Even though a series of strict steelmaking and refining process measures have been applied so far to decrease the concentrations of Ti and N, micrometer-scale TiN inclusions can be still observed in the tire cord steel samples.<sup>[7]</sup> With the tire cord steel strength improving through increasing carbon content, *e.g.*, from 0.7 to 0.9 wt pct, the hazards of TiN inclusion for the material properties of steel products would become more serious.<sup>[8,9]</sup> Therefore, how to control the precipitation of TiN inclusion has become an urgent issue in the steelmaking industry.

PENG WANG is with the The State Key Laboratory of Refractories and Metallurgy, Wuhan University of Science and Technology, Wuhan, 430081, P.R. China. CHENGZHI LI, LU WANG, JUHUA ZHANG, and ZHENGLIANG XUE are with the The State Key Laboratory of Refractories and Metallurgy, Wuhan University of Science and Technology and also with the Key Laboratory for Ferrous Metallurgy and Resources Utilization of Ministry of Education, Wuhan University of Science and Technology, Wuhan, 430081, P.R. China. Contact e-mail: chengzhi.li@wust.edu.cn; xuezhengliang@wust.edu.cn

Manuscript submitted November 17, 2020, accepted April 1, 2021.

Article published online April 27, 2021.

To look inside the mechanisms of TiN precipitation and growth behavior during solidification, a series of thermodynamic and kinetic studies has been conducted in former studies.<sup>[10–14]</sup> In these studies, various kinds of solute micro-segregation models (*e.g.*, Scheil model, Lever-rule model and Ohnaka model, *etc.*) were used to quantify the enrichment of Ti and N during solidification. Then by calculating the actual activity product of TiN and the equilibrium activity product which is a function of the temperature at solidifying front, the solidification fraction at which TiN starts precipitating was thermodynamically determined. However, in these studies, the micro-segregations of other solute elements, such as carbon, phosphorus, and sulfur, were rarely taken into account. In fact, during the solidification of molten steel, the concentration of each solute element keeps varying in the inter-dendrite space due to micro-segregation. The variations in the solute concentrations would affect the thermodynamic calculation of TiN precipitation *via* affecting the liquidus and solidus temperatures of steel, the activity coefficients of Ti and N, and other thermodynamic parameters. Within each solidification fraction step, these variations would definitely affect the solute micro-segregations in its next step. Therefore, this iterative influence on the thermodynamic calculation of TiN precipitation would be non-negligible.

In this paper, the thermodynamic calculation of TiN precipitation in SWRH92A super-strength high carbon tire cord steel is conducted, especially considering the micro-segregations of carbon and other solute elements during the solidification of molten steel. Furthermore, the TiN precipitation calculation is coupled with the calculations of the Ti and N micro-segregations at the late stage of solidification to mimic the actual precipitation of TiN. In the end, the radius of the precipitated TiN inclusion is calculated based on the thermodynamic calculation results. The TiN particle size is compared with the values measured in the metallographic images published in previous studies to prove the calculation reasonability.

## II. THERMODYNAMIC THEORY OF TIN PRECIPITATION

### A. Basic Thermodynamic Condition of TiN Precipitation

The chemical reaction of TiN formation in molten steel and the corresponding standard Gibbs free energy change are expressed as follows<sup>[15]</sup>:

$$\begin{aligned} [\text{Ti}] + [\text{N}] &= \text{TiN}_{(s)} \\ \Delta G^\theta &= -RT \cdot \ln K_{\text{TiN}} \\ &= -291,000 + 107.91T (\text{J mol}^{-1}) \end{aligned} \quad [1]$$

where  $K_{\text{TiN}}$  denotes the reaction equilibrium constant;  $R$  is the ideal gas constant with value of 8.314 J/(mol K);  $T$  is the temperature of molten steel,  $K$ . During the precipitation of TiN inclusion, the actual change of Gibbs free energy can be calculated as follows:

$$\begin{aligned} \Delta G &= \Delta G^\theta + RT \ln \frac{a_{\text{TiN}}}{a_{[\text{Ti}]} \cdot a_{[\text{N}]}} \\ &= \Delta G^\theta + RT \ln \frac{1}{f_{\text{Ti}} \cdot \omega_{[\text{Ti}]} \cdot f_{\text{N}} \cdot \omega_{[\text{N}]}} \end{aligned} \quad [2]$$

where  $a_{\text{TiN}}$ ,  $a_{[\text{Ti}]}$ , and  $a_{[\text{N}]}$  denote the activities of TiN, Ti, and N in molten steel, respectively. For pure TiN inclusion,  $a_{\text{TiN}} = 1$ .  $\omega_{[\text{Ti}]}$  and  $\omega_{[\text{N}]}$  denote the mass fractions of Ti and N in molten steel, respectively;  $f_{[\text{Ti}]}$  and  $f_{[\text{N}]}$  denote the activity coefficients of Ti and N, respectively. The values of  $f_{[\text{Ti}]}$  and  $f_{[\text{N}]}$  can be calculated by Eqs. [3] and [4]<sup>[16]</sup>:

$$\lg f_{[\text{Ti}]} = \lg f_{[\text{Ti}]}^{1873\text{K}} \cdot \left( \frac{2557}{T} - 0.365 \right) \quad [3]$$

$$\lg f_{[\text{N}]} = \lg f_{[\text{N}]}^{1873\text{K}} \cdot \left( \frac{3280}{T} - 0.75 \right) \quad [4]$$

where  $f_{[\text{Ti}]}^{1873\text{K}}$  and  $f_{[\text{N}]}^{1873\text{K}}$  are the activity coefficients of Ti and N at 1873 K, which can be calculated by Eqs. [5] and [6]:

$$\lg f_{[\text{Ti}]}^{1873\text{K}} = \sum e_{\text{Ti}}^i \cdot \omega_{[i]} \quad [5]$$

$$\lg f_{[\text{N}]}^{1873\text{K}} = \sum e_{\text{N}}^i \cdot \omega_{[i]} \quad [6]$$

where  $e_{\text{Ti}}^i$  and  $e_{\text{N}}^i$  are the interaction coefficients of solute element  $i$  for Ti and N at 1873 K, respectively. For the studied SWRH92A tire cord steel, its main chemical composition is shown in Table I. The specific values of first-order interaction coefficients of the main solute elements in the molten steel for Ti and N at 1873 K are listed in Table II.<sup>[16,17]</sup> Since the mass fraction of Fe in molten steel is more than 90 wt pct, the impact of second-order interaction coefficients can be ignored.

By combining Eqs. [1] through [6], it can be seen that with the temperature of molten steel decreasing during the solidification process, the actual Gibbs free energy change  $\Delta G$  varies as well. When  $\Delta G \leq 0$ , the precipitation of TiN is thermodynamically possible. Based on the combination of Eqs. [1] and [2], the thermodynamic condition of TiN precipitation is expressed as follows:

$$K_{\text{TiN}} \geq \frac{1}{f_{\text{Ti}} \cdot \omega_{[\text{Ti}]} \cdot f_{\text{N}} \cdot \omega_{[\text{N}]}} \quad [7]$$

By introducing the activity product of TiN,  $Q_{\text{TiN}}$ , and defining  $K'_{\text{TiN}}$  as the reciprocal of  $K_{\text{TiN}}$ , Eq. [7] can be reformulated as follows:

$$K'_{\text{TiN}} \leq Q_{\text{TiN}} = f_{\text{Ti}} \cdot \omega_{[\text{Ti}]} \cdot f_{\text{N}} \cdot \omega_{[\text{N}]} \quad [8]$$

The equilibrium activity product  $K'_{\text{TiN}}$  is a function of the temperature at the solid–liquid mushy zone in a dendrite cell,  $T_{s-1}$ .  $Q_{\text{TiN}}$  is the product of the concentrations and activity coefficients of Ti and N. Due to

**Table I. Chemical Composition of Studied SWRH92A Tire Cord Steel, Wt Pct**

Elements	C	Si	Mn	P	S	O	Ti	N
Content	0.92	0.18	0.51	0.018	0.0064	0.0018	0.0005	0.0043

**Table II. First-Order Interaction Coefficients  $e_j^i$  of Solute Elements in Molten Steel at 1873 K.<sup>[16,17]</sup>**

$e_j^i(i \rightarrow)$	C	Si	Mn	P	S	O	Ti	N
$e_{Ti}^i$	-0.165	0.05	0.0043	-0.064	-0.11	-1.8	0.013	-1.8
$e_N^i$	0.13	0.047	-0.021	0.045	0.007	0.05	-0.53	0

the micro-segregations of solute elements, the concentrations of solute elements are not constants as the original values shown in Table I, but variants during solidification. Therefore, the key points of solving Eq. [8] are the accurate determinations of  $T_{s-1}$  and the real-time solute concentrations during solidification.

### B. Calculation of $T_{s-1}$ During Solidification of Molten Steel

Based on the previous thermodynamic studies,  $T_{s-1}$  is a function of liquidus temperature,  $T_l$ , solidus temperature,  $T_s$ , and solidification fraction,  $g$ . The specific relationship is expressed as Eq. [9]<sup>[18]</sup>:

$$T_{s-1} = T_m - \frac{T_m - T_l}{1 - g \cdot \frac{T_l - T_s}{T_m - T_s}} \quad [9]$$

where  $T_m$  is the melting point of pure iron (1811 K). The values of  $T_l$  and  $T_s$  are usually estimated based on the following empirical expressions:

$$T_l = T_m - \sum \Delta t_l \cdot \omega_{[i]} \quad [10]$$

$$T_s = T_m - \sum \Delta t_s \cdot \omega_{[i]} \quad [11]$$

where  $\Delta t_l$  and  $\Delta t_s$  denote the reduced temperature values for solute element  $i$  of 1.0 wt pct. The detailed formation is listed in Table III.<sup>[16]</sup>

Based on Eqs. [10] and [11] and Table III, it can be seen that the concentrations of solute elements significantly affect the values of  $T_l$  and  $T_s$  of molten steel and thus further affect  $T_{s-1}$  during solidification. The studied SWRH92A high carbon tire cord steel has a relatively high carbon content (> 0.9 wt pct) and, therefore, the effect of carbon enrichment due to micro-segregation in the inter-dendrite space on  $T_l$  and  $T_s$  is paid particular attention. Figure 1 shows an example comparison of  $T_l$  and  $T_s$  of SWRH92A steel between the calculation cases considering and not considering carbon enrichment. In the carbon segregation case (Case 1), Lever-rule model is used for calculating the carbon micro-segregation ratio. The comparison results indicate that because of

**Table III. Values of  $\Delta t_l$  and  $\Delta t_s$  for Solute Elements in Molten Steel, K<sup>[16]</sup>**

Element	C	Si	Mn	P	S	O	Ti	N
$\Delta t_l$	65	8	5	30	25	80	20	90
$\Delta t_s$	175	20	30	280	575	160	40	—

carbon enrichment in Case 1, there are obvious decreasing trends in  $T_l$  and especially  $T_s$  with increasing solidification fraction, which causes a more significant drop of  $T_{s-1}$  compared with the trend of  $T_{s-1}$  in Case 2. The decreased  $T_{s-1}$  at a certain solidification fraction would undoubtedly affect the precipitation equilibrium of TiN and thus shift the precipitation point along the solidification fraction axis. Furthermore, the decrease in  $T_{s-1}$  also affects the calculations of other thermodynamic parameters, *e.g.*, the diffusion coefficients and activity coefficients of solute elements. Since the values of  $T_l$  and  $T_s$  during solidification are closely related to the real-time concentrations of solute elements, as shown in Eqs. [10] and [11], the accurate determination of the segregated solute concentrations in the dendrite cell zone becomes the most important part in the thermodynamic calculation.<sup>[19]</sup>

### C. Micro-segregation Models for Solute Elements

During the actual solidification of molten steel, the redistribution of solute atoms takes place because of the solubility difference between the solid and liquid phases. As a result, the micro-segregation of solute element occurs between the dendrite arms. The enrichment of solute element occurring in the inter-dendrite liquid pools can be quantified by the segregation ratio which is defined as the ratio of the segregated solute concentration in liquid phase to its original value. To date, there have been several models proposed for calculating the segregation ratio of solute elements. In these models, solute elements are assumed to diffuse completely in liquid phase. While, regarding the solute diffusion in

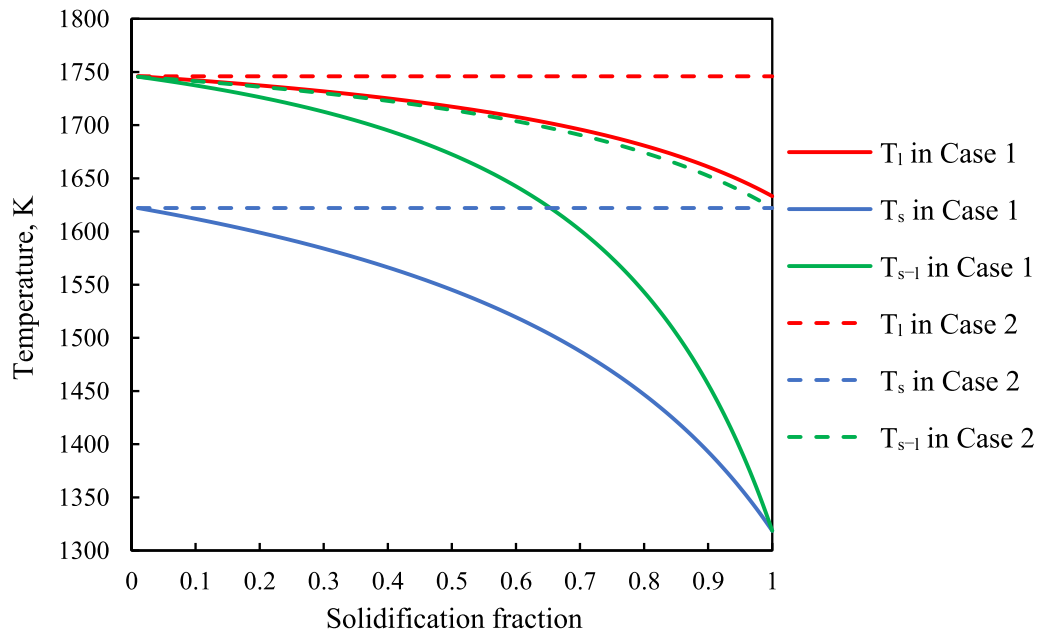


Fig. 1—Comparison of  $T_1$ ,  $T_s$ , and  $T_{s-1}$  between the calculation cases considering (Case 1) and not considering (Case 2) carbon micro-segregation during solidification.

solid phase, the model assumptions are categorized into three types, *i.e.*, (I) complete diffusion; (II) no diffusion; and (III) partial diffusion. For each Category III model, the method of calculating the partial diffusion in solid phase differs. A summary of the micro-segregation models for solute elements during solidification is shown in Table IV.

In some former studies,<sup>[8,25–27]</sup> the combination of Lever-rule and Scheil models (generally called LRSM) is used. In LRSM, the solute elements are applied to either Lever-rule model or Scheil model according to their diffusion coefficients in solid phase,  $D_i^s$ . For example,  $D_{Ti}^s$  is normally much lower than  $D_N^s$  over the solidification process. So the segregated concentration of Ti is calculated using Scheil model and that of N using Lever-rule model. LRSM provides a convenient way of choosing segregation models for solute elements, but this combination of extreme models would inevitably overestimate or underestimate the actual segregated concentrations of the studied elements. This is because in the actual solidification process, the diffusion of one solute element in solid phase can be neither absolutely complete nor negligible. Some solute elements may be neither suitable for Scheil model nor Lever-rule model due to their intermediate values of  $D_i^s$ , and thus the usage of LRSM may lead to a significant deviation from the real segregated solute concentration.

Compared to Category I and II models, Category III models considering partial element diffusion in solid phase are relatively moderate and flexible. The advantage of Category III models is their flexibility and wide applicability for the inclusion precipitation calculations. The main features of three typical Category III models are simply discussed as below. Brody–Fleming model is proposed based on the analysis of Scheil model and first takes the finite diffusion in solid phase into account by

introducing back diffusion coefficient ( $\alpha$  in Table I). When  $\alpha$  equals to 0 and 0.5 (*i.e.*,  $\phi$  is equal to 0 and 1), this model would become the Scheil model and the Lever-rule model, respectively. However, for some interstitial solutes with high  $D_i^s$ , the values of  $\alpha$  may be higher than 0.5 and this would make the calculated segregated concentration unreasonable. This limitation is overcome by the Clyne–Kurz model where  $\phi$  is reformulated based on an approximate analytical treatment of the back diffusion. With this treatment, when  $\alpha$  equals to 0 and infinite, the model approaches to the Scheil model and the Lever-rule model, respectively. Ohnaka model analyses the solute redistribution during solidification by a profile method which approximately considers the two-dimensional diffusion in solid phase. In this model, the columnar and plate dendrites are, respectively, considered and hence the two  $\phi$  expressions are, respectively, provided in Table I. Note that in this study, the dendrites are assumed as columnar, so  $\phi_2$  is used in the following calculations by Ohnaka model. Although all these three models assume incomplete solute back diffusion in solid phase, the different expressions of  $\phi$  would theoretically result in different segregated solute concentrations. Therefore, the selection of appropriate segregation model for each solute element is worth being discussed.

#### D. Discussion of Applicability of Category III MODELS for Solute Elements

For this thermodynamic calculation of TiN precipitation in SWRH92A tire cord steel, eight main solute elements are considered, which are carbon, silicon, manganese, phosphorous, sulfur, titanium, nitrogen, and oxygen. The expression of  $D_i^s$  as a function of  $T_{s-1}$ , together with the solid/liquid equilibrium partition



**Table IV. Summary of Micro-segregation Models for Solute Elements During Solidification**

Model Name	Model Expression	Model Description
Category I: Lever-Rule Model [20]	$\frac{\omega_{[i]}}{\omega_{[i]}^0} = [1 - (1 - k_i)g]^{-1}$	complete diffusion in solid phases
Category II: Scheil Model [21]	$\frac{\omega_{[i]}}{\omega_{[i]}^0} = (1 - g)^{(k_i-1)}$	no diffusion in solid phase
Category III	$\frac{\omega_{[i]}}{\omega_{[i]}^0} = [1 - (1 - \Phi k_i)g]^{(k_i-1)/(1-\Phi k_i)}$	partial diffusion in solid phase; Parameter $\Phi$ is introduced in Category III models. $\Phi \in (0, 1)$ ; $\Phi = 1$ , the models are equal to Lever-rule model; $\Phi = 0$ , the models are equal to Scheil model.
Brody–Fleming Model [22]	$\Phi = F(\alpha); \quad a = 4D_i^s \tau / \lambda^2$ $\Phi = 2\alpha$	
Clyne–Kurz Model [23]	$\Phi = 2\alpha \left(1 - e^{-\frac{1}{2\alpha}}\right) - e^{-\frac{1}{2\alpha}}$	
Ohnaka Model [24]	$\Phi_1 = \frac{2\alpha}{1+2\alpha}; \quad \Phi_2 = \frac{4\alpha}{1+4\alpha}$	

Note  $k_i$  is partition coefficient of element  $i$ ;  $D_i^s$  is the diffusion coefficient of element  $i$  in solid phase,  $\text{cm}^2 \text{s}^{-1}$ ;  $\tau$  is the local solidification time, s;  $\lambda$  is the secondary dendrite arm space, cm;  $\alpha$  is back diffusion coefficient;  $\Phi_1$  is for the plate dendrite case;  $\Phi_2$  is for the columnar dendrite case.

**Table V. Equilibrium Partition Coefficients Between Solid and Liquid Steel of Solute Element and Their Diffusion Coefficients in Solid Phase.** [17,28,29]

Element	$k_i$	$D_i^s$ ( $\text{cm}^2 \text{s}^{-1}$ )
C	0.34	$0.076 \exp(-143,511/(RT_{s-1}))$
Si	0.52	$0.3 \exp(-251,458/(RT_{s-1}))$
Mn	0.78	$0.055 \exp(-249,366/(RT_{s-1}))$
P	0.13	$0.01 \exp(-182,841/(RT_{s-1}))$
S	0.035	$2.4 \exp(-223,425/(RT_{s-1}))$
Ti	0.32	$0.15 \exp(-250,000/(RT_{s-1}))$
N	0.48	$0.91 \exp(-168,600/(RT_{s-1}))$
O	0.025	$5.75 \exp(-168,700/(RT_{s-1}))$

Note  $R = 8.314 \text{ J/(mol K)}$  and the unit of  $T_{s-1}$  is Kelvin. Herein, the solid phase of steel refers to  $\gamma\text{-Fe}$ .

coefficient  $k_i$ , of each studied element is shown in Table V. [28–30] Herein, the solid phase of steel refers to  $\gamma\text{-Fe}$  because the original carbon content of the studied steel is 0.92 wt pct, and based on the iron-carbon equilibrium diagram, only  $\gamma\text{-Fe}$  will be formed during the whole solidification process. The back diffusion coefficients of these solute elements during solidification are first compared in Figure 2 under the condition that the effect of solute micro-segregation on the liquidus and solidus temperatures of molten steel is temporally neglected. The comparison in Figure 2 indicates that sequence of  $D_i^s$  of the studied solute elements is  $O \gg N > C >$  other solute elements (*i.e.*, Si, Mn, P, S and Ti). Based on this sequence, it is clear that oxygen, nitrogen, and carbon have relatively high values of  $D_i^s$  and in comparison, the remaining five solute elements have relatively lower diffusivity in solid phase.

To investigate the appropriate Category III models for each element, the values of  $\phi(\alpha)$  calculated by different segregation models are further compared. To do this comparison, the local solidification time,  $\tau$ , and the secondary dendrite arm space,  $\lambda$ , should be calculated beforehand, as shown in Table IV. The expressions of  $\tau$  and  $L$  are given in Eqs. [12] and [13], respectively. [30,31]

$$\tau = (T_l - T_s) / R_c \quad [12]$$

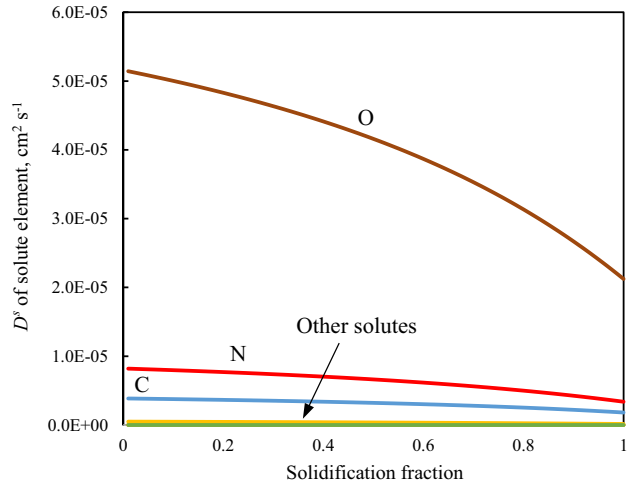


Fig. 2—Comparison of  $D_i^s$  for the studied solute elements during solidification provided that the effect of element segregation on  $T_l$  and  $T_s$  is not considered.

$$\lambda = 143.9 R_c^{-0.3616} \cdot \omega_C^{(0.5501 - 1.996 \cdot \omega_C)} \quad [13]$$

where  $R_c$  is the cooling rate of molten steel, K/s. In this test case,  $R_c$  is set as 1.67 K/s. The original carbon concentration is temporarily substituted into  $\omega_C$  in Eq. [13]. The detailed comparison of  $\phi(\alpha)$  calculated by Brody–Fleming (abbrev. B–F), Clyne–Kurz (abbrev. C–K), and Ohnaka models for each solute element is shown in Figure 3.

The comparison results in Figure 3 mainly indicate two conclusions. First, for the solute elements with high diffusivity in solid phase (*i.e.*, C, N and O), B–F model generally predicts an unreasonable higher  $\phi(\alpha)$  than C–K and Ohnaka models, and the other two models predict the very close values of  $\phi(\alpha)$  near 1.0. Second, for the solute elements with low diffusivity in solid phase (*i.e.*, Si, Mn, P and Ti), the values of  $\phi(\alpha)$  calculated by all three models are generally low. Among them, B–F and C–K models almost predict the same value and in comparison Ohnaka model provides a relatively higher

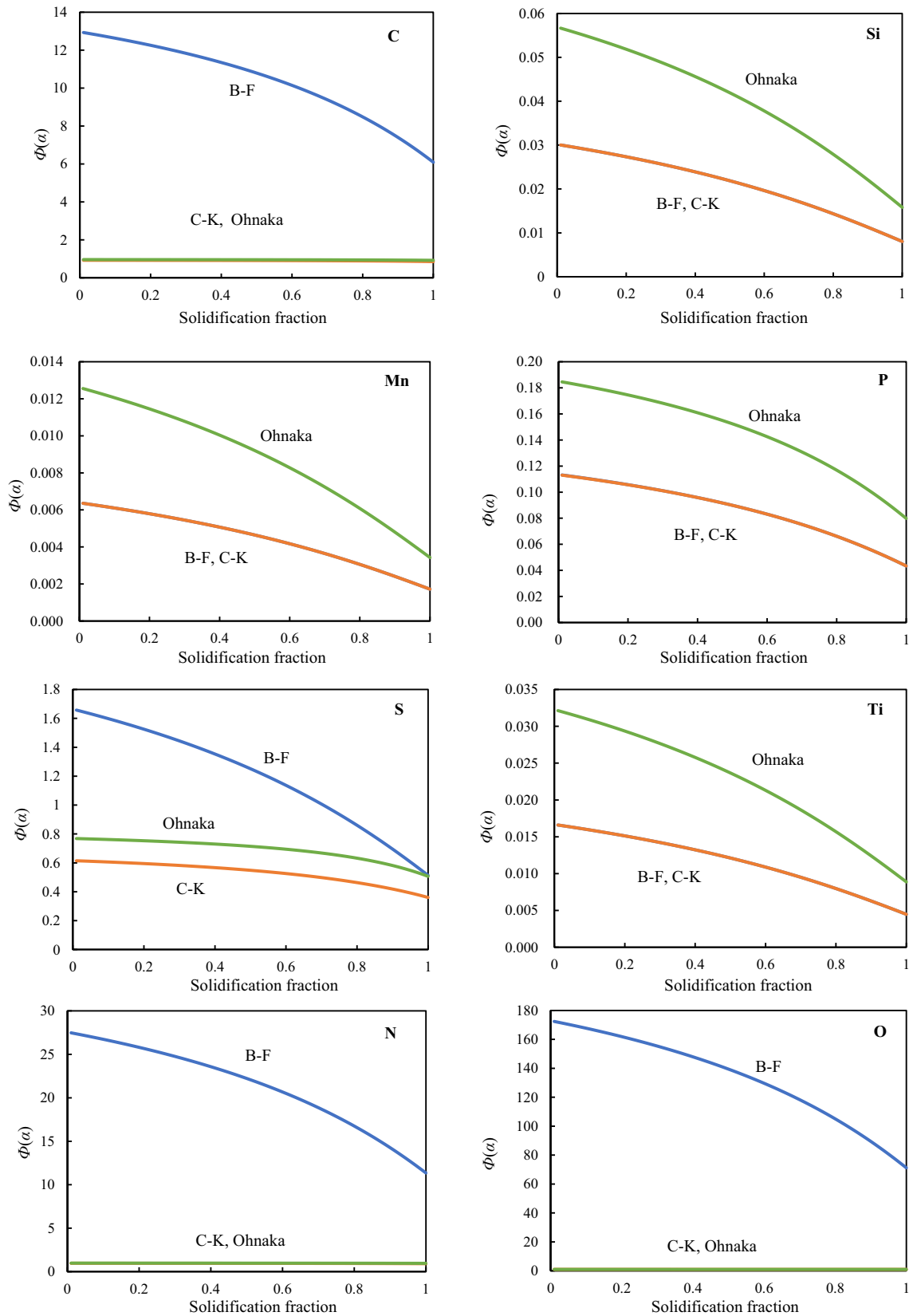


Fig. 3—Comparison of  $\phi(x)$  calculated by Brody–Fleming, Clyne–Kurz, and Ohnaka models for each solute element.

$\phi(x)$ . For S which has an intermediate diffusivity, the values of  $\phi(x)$  calculated by C–K and Ohnaka models

keep lower than 1.0 over the solidification process but differ slightly. Therefore, for C, N and O, either C–K or

Ohnaka model can be used in the segregation calculation. For Si, Mn, P and Ti, either C–K (or B–F) or Ohnaka model is applicable. Based on the above analysis, a summary is shown in Table VI.

In general, both C–K and Ohnaka models are applicable for all the studied solute elements and these two models can be even regarded as equivalent for the elements of C, N, and O. While for the remaining elements, it is difficult to determine which model is more appropriate. Considering this issue, C–K and Ohnaka models are, respectively, applied to the following thermodynamic calculations in this study and then the corresponding calculation results will be compared between these two model cases

### III. CALCULATION PROCEDURES OF TiN PRECIPITATION AND GROWTH

#### A. Thermodynamic Calculation of Solute Micro-segregation

The calculation unit starts from the center axis of one secondary dendrite in the mushy zone and ends at the length of half secondary dendrite arm space, as shown in Figure 4. Through applying the finite volume method, the calculation proceeds by every solidification fraction of 0.001,  $\Delta g$ . In each calculation step, the solidification is assumed at a steady state where the temperature of molten steel and solute concentrations are uniform. As solidification proceeds, the solid–liquid interface slowly moves towards the center of the inter-dendrite liquid pool.

The variations in solute concentrations due to the solute micro-segregations during solidification would consequently keep updating the values of  $T_{s-1}$ ,  $D_i^s$ ,  $\tau$ ,  $\lambda$  and  $f_i$  in the calculation. Based on Eq. [9],  $T_{s-1}$  is a function of the liquidus and solidus temperatures ( $T_l$ ,  $T_s$ ) which are normally estimated via the actual concentrations of solute elements, as shown in Eqs. [10] and [11]. As the solute concentrations vary,  $T_l$  and  $T_s$  would keep changing and this change further affects the value of  $T_{s-1}$ . As a result, the updated  $T_{s-1}$ ,  $T_l$  and  $T_s$  affect the values of  $D_i^s$  and  $\tau$  based on the expressions shown in Table V and Eq. [12].  $\lambda$  is a function of actual carbon concentration (see Eq. [13]) so the secondary dendrite arm space also keeps varying during the solidification. Furthermore,  $f_i$  is also a variant according to Eqs. [3] through [6].

As the calculation proceeds by  $\Delta g$ , the values  $T_l$ ,  $T_s$  and  $\lambda$  are first updated by the segregated solute concentrations calculated in the previous step (for the first step, the original concentrations are used), then  $T_{l-s}$ ,

$f_i$ ,  $D_i^s$  and  $\tau$  are updated, followed by the update of back diffusion coefficient,  $\alpha$ . Finally, the segregated solute concentrations in this step are calculated by segregation model. In each step, the calculated activity product of TiN (*i.e.*,  $Q_{TiN}$  in Eq. [7]) is compared with the equilibrium activity product  $K'_{TiN}$  which is a function of  $T_{s-1}$  to determine the solidification fraction at which TiN precipitation starts,  $g_{TiN}$ . Figure 5 shows the thermodynamic calculation procedure as solidification fraction increases by  $\Delta g$ . The whole calculation process ( $0 \rightarrow g \rightarrow 1$ ) is conducted using the commercial software MATLAB.

#### B. Coupling of Micro-segregation and TiN Precipitation

If  $Q_{TiN} > K'_{TiN}$  is detected in one calculation step, TiN starts precipitating and then grows up in the following calculation steps. As a result, the concentrations of Ti and N in the molten steel would be partially consumed. This is realized in the thermodynamic calculation by coupling the TiN precipitation module with the solute micro-segregation module. In this study, the precipitated TiN inclusions are assumed to be uniformly

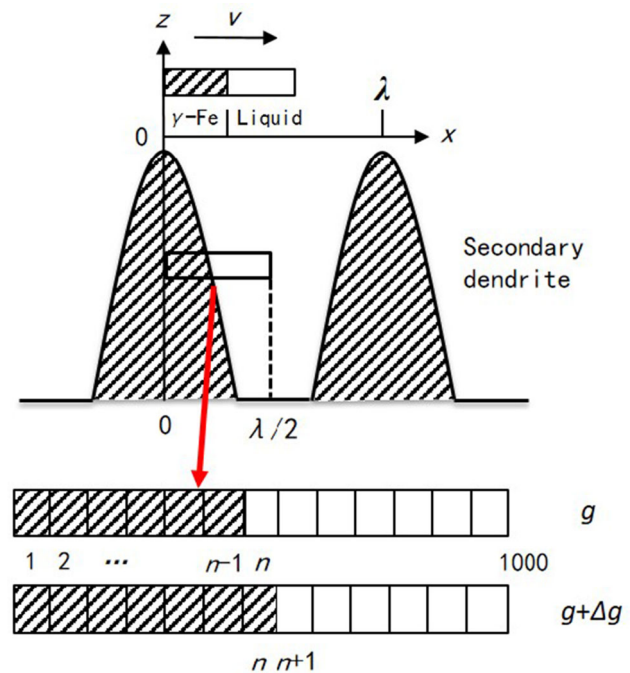


Fig. 4—Schematic of calculation unit considered in the finite volume method and the illustration of the solidification of sub-unit  $i$  within  $\Delta t$ .

Table VI. Summary of the Applicability of Category III Models for Solute Element

Element Group	Brody–Fleming Model		Clyne–Kurz Model		Ohnaka Model
C, N, O	not applicable		applicable	↔	applicable
Si, Mn, P, Ti	applicable	↔	applicable		applicable
S	not applicable		applicable		Applicable

Note The double-headed arrow indicates that the models can be regarded as equivalent for the certain group of elements.

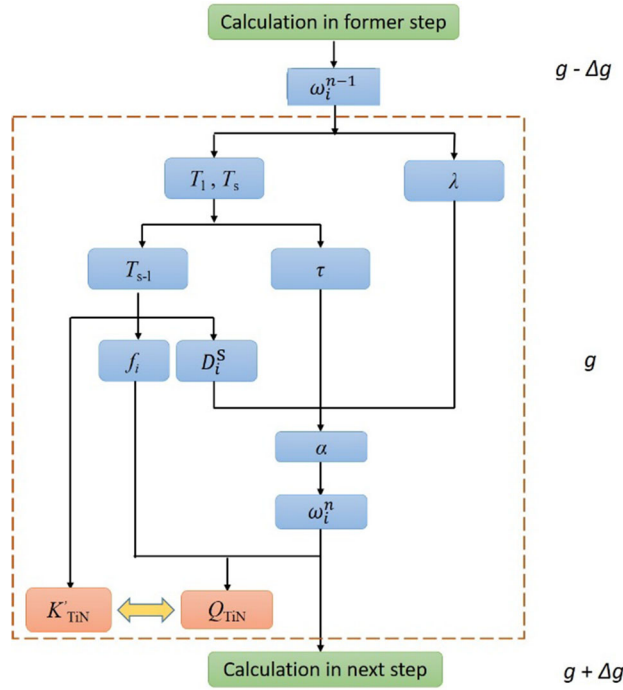


Fig. 5—Illustration of thermodynamic calculation procedure as solidification fraction increases by  $\Delta g$ .

dispersed in the liquid phase. When TiN precipitation occurs, there exists an equilibrium between the inclusion and liquid steel phases, which can be expressed by the following equations<sup>[32,33]</sup>:

$$f_{\text{Ti}} \cdot (\omega_{[\text{Ti}]} - \Delta\omega_{[\text{Ti}]}) \cdot f_{\text{N}} \cdot (\omega_{[\text{N}]} - \Delta\omega_{[\text{N}]}) = K'_{\text{TiN}} \quad [14]$$

$$\Delta\omega_{[\text{Ti}]} / \Delta\omega_{[\text{N}]} = M_{\text{Ti}} / M_{\text{N}} \quad [15]$$

where  $\Delta\omega_{[\text{Ti}]}$  and  $\Delta\omega_{[\text{N}]}$  are the consumed Ti and N concentrations due to TiN precipitation, respectively;  $M_{\text{Ti}}$  and  $M_{\text{N}}$  are molar mass of Ti and N, respectively. After TiN precipitates within one calculation step, Ti and N would reach their equilibrium concentrations, respectively, in the molten steel. Equation [14] can be also reformulated as:

$$f_{\text{Ti}} \cdot \omega_{[\text{Ti}]}^e \cdot f_{\text{N}} \cdot \omega_{[\text{N}]}^e = K'_{\text{TiN}} \quad [16]$$

where  $\omega_{[\text{Ti}]}^e$  and  $\omega_{[\text{N}]}^e$  are the equilibrium concentrations of Ti and N, respectively, which is equal to  $(\omega_{[\text{Ti}]} - \Delta\omega_{[\text{Ti}]})$  and  $(\omega_{[\text{N}]} - \Delta\omega_{[\text{N}]})$ , respectively.

The values of  $\omega_{[\text{Ti}]}$  and  $\omega_{[\text{N}]}$  in Eq. [14] are obtained based on the Ti and N micro-segregation calculations by segregation model. Before TiN starts precipitation, Ti and N are continuously enriched in the inter-dendrite space. In  $(n-1)$ th and  $n$ th calculation steps, the segregated concentrations of either Ti or N are normally calculated by the general expression of Category III models:

$$\omega_{[i]}^n = \omega_{[i]}^0 \cdot [1 - (1 - \Phi_{(n)}k_i)g]^{(k_i-1)/(1-\Phi_{(n)}k_i)} \quad [17]$$

$$\omega_{[i]}^{n-1} = \omega_{[i]}^0 \cdot [1 - (1 - \Phi_{(n-1)}k_i)g]^{(k_i-1)/(1-\Phi_{(n-1)}k_i)} \quad [18]$$

where  $\omega_{[i]}^{n-1}$  and  $\omega_{[i]}^n$  are the segregated concentrations of Ti or N in the  $(n-1)$ th and  $n$ th steps, respectively;  $\omega_{[i]}^0$  refers to the original concentration of Ti or N;  $\Phi_{(n-1)}$  and  $\Phi_{(n)}$  are the values of  $\phi(x)$  calculated in the  $(n-1)$ th and  $n$ th steps, respectively;  $k_i$  represents for the partition coefficient of Ti or N and its value is assumed to be constant during the solidification process. By combining Eqs. [17] and [18],  $\omega_{[i]}^n$  can be expressed as follows:

$$\omega_{[i]}^n = \omega_{[i]}^{n-1} \cdot \frac{[1 - (1 - \Phi_{(n)}k_i)g]^{(k_i-1)/(1-\Phi_{(n)}k_i)}}{[1 - (1 - \Phi_{(n-1)}k_i)g]^{(k_i-1)/(1-\Phi_{(n-1)}k_i)}} \quad [19]$$

Note that in the TiN precipitation module, the actual concentration of Ti or N in the  $(n-1)$ th step,  $\omega_{[i]}^{n-1}$ , would finally reach the corresponding equilibrium concentration,  $\omega_{[i]}^e$ , in the  $(n-1)$ th step instead of the segregated value calculated by Eq. [18].

### C. Kinetic Calculation of TiN Inclusion Growth

To estimate the TiN inclusion size at the end of solidification, the principal mechanism controlling the growth rate of TiN should be clear. In general, the potential mechanisms that control the growth rate of TiN include the chemical reaction rate at the TiN/steel interface and the mass transport rates of Ti and N from the liquid phase to the interface. The interfacial reaction rate within the molten steel temperature range is very fast so the inclusion growth is assumed to be diffusion-controlled. The diffusion coefficients of Ti and N in the molten steel are, respectively, calculated as follows<sup>[34]</sup>:

$$D_{\text{Ti}}^L (\text{m}^2 \text{s}^{-1}) = 3.10 \times 10^{-7} \exp(-11500/(RT_{s-l})) \quad [20]$$

$$D_{\text{N}}^L (\text{m}^2 \text{s}^{-1}) = 3.25 \times 10^{-7} \exp(-11500/(RT_{s-l})) \quad [21]$$

Equations [20] and [21] indicate that  $D_{\text{Ti}}^L$  and  $D_{\text{N}}^L$  are very close within the molten steel temperature range. Since the original concentration of Ti in the molten steel is lower than the value of N by an order of magnitude, as shown in Table I, the diffusion of Ti can be assumed as the controlling mechanism for the growth rate of TiN inclusion.

According to the previous kinetics research,<sup>[35]</sup> the diffusion flux of Ti towards the TiN particle is proportional to the Ti concentration gradient, so for a TiN particle with the radius of  $r$ , there is

$$J_{\text{Ti}} = \frac{D_{\text{Ti}}^L \cdot \rho_{\text{Fe}}}{100M_{\text{Ti}} \cdot r} \cdot (\omega_{[\text{Ti}]} - \omega_{[\text{Ti}]}^e) \quad [22]$$



where  $J_{\text{Ti}}$  is the diffusion flux of Ti,  $\text{mol m}^{-2} \text{s}^{-1}$ ;  $r$  is the radius of TiN particle, m;  $\rho_{\text{Fe}}$  is the iron density ( $7.07 \times 10^3 \text{ kg m}^{-3}$ ), and  $M_{\text{Ti}}$  is the molecular weight of Ti ( $0.048 \text{ kg mol}^{-1}$ ).  $\omega_{[\text{Ti}]}$  is the Ti concentration calculated by the coupling of Ti micro-segregation and TiN precipitation during solidification, wt pct, and  $\omega_{[\text{Ti}]}^e$  is the Ti concentration in equilibrium with TiN particle, wt pct. Assuming that the TiN particle is spherical and each TiN particle grows independently without interaction with others at a stationary diffusion state, the relationship between the Ti diffusion flux and the TiN particle radius is expressed by Eq. [23]:

$$4\pi r^2 \cdot M_{\text{TiN}} \cdot J_{\text{Ti}} \cdot \Delta t = \frac{4}{3} \pi \rho_{\text{TiN}} \cdot [(r + \Delta r)^3 - r^3] \quad [23]$$

where  $M_{\text{TiN}}$  is the molecular weight of TiN ( $0.062 \text{ kg mol}^{-1}$ ),  $\rho_{\text{TiN}}$  is the TiN density ( $5.43 \times 10^3 \text{ kg m}^{-3}$ ),  $\Delta t$  refers to the unit growing time, s, and  $\Delta r$  denotes the increase in TiN particle radius within  $\Delta t$ , m. Combining Eqs. [22] and [23], the growth of TiN particle can be expressed by Eq. [24]:

$$r \frac{dr}{dt} = \frac{M_{\text{TiN}} \cdot \rho_{\text{Fe}}}{100 M_{\text{Ti}} \cdot \rho_{\text{TiN}}} \cdot D_{\text{Ti}}^L \cdot (\omega_{[\text{Ti}]} - \omega_{[\text{Ti}]}^e) \quad [24]$$

Through integration for  $r$  and  $t$  in Eq. [24], the radius of TiN particle can be calculated by Eq. [25]:

$$\int_0^{r_t} r dr = \frac{M_{\text{TiN}} \cdot \rho_{\text{Fe}}}{100 M_{\text{Ti}} \cdot \rho_{\text{TiN}}} \cdot \int_0^t D_{\text{Ti}}^L \cdot (\omega_{[\text{Ti}]} - \omega_{[\text{Ti}]}^e) dt \quad [25]$$

where  $r_t$  refers to the radius of TiN particle after time  $t$  since the TiN precipitation starts. Note that  $D_{\text{Ti}}^L$  actually varies with the TiN growth time,  $t$ , due to the variation in the temperature of molten steel, as shown in Eq. [20], and the driving force for TiN precipitation,  $(\omega_{[\text{Ti}]} - \omega_{[\text{Ti}]}^e)$ , in each calculation step is also a variant with growth time,  $t$ . Therefore, these two parameters should be treated as functions of growth time rather than constants. Although  $\rho_{\text{Fe}}$  actually also changes during solidification, its value is temporarily regarded as a constant in this study for calculation simplicity.

In general, the overall calculation procedures described in Section III are shown in Figure 6. Please note an assumption that in the current calculation model, the precipitations of other types of inclusions from liquid steel during solidification are currently not considered. In reality, for the chemical composition of the studied SWRH92A tire cord steel, it is thermodynamically possible that other types of inclusions may also precipitate sequentially during the solidification process.<sup>[36]</sup> As a result, the consumptions of the constituent solute elements would affect the calculated solute concentrations.<sup>[37]</sup> In our future work, the calculation model will be improved by taking this influence into account.

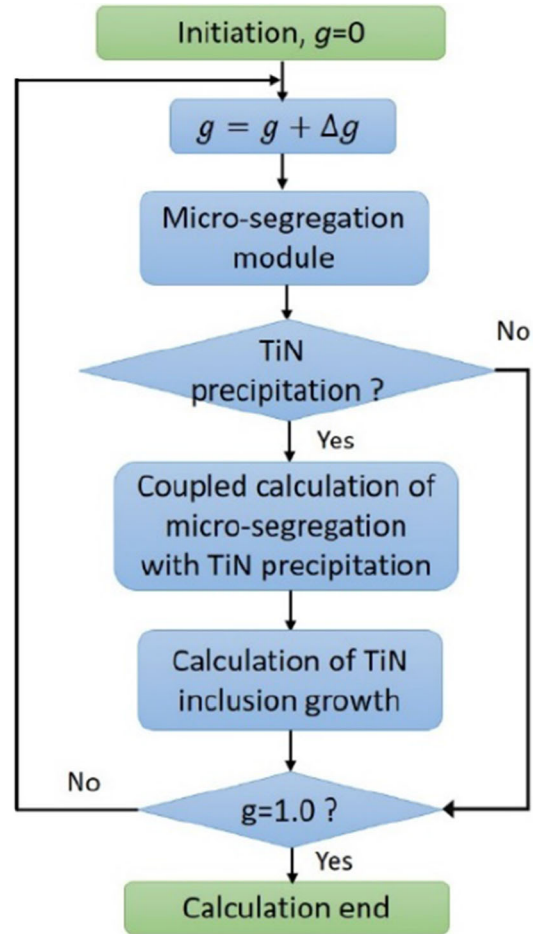


Fig. 6—Overall flow chart of TiN precipitation calculation in the molten steel during solidification.

## IV. RESULTS AND DISCUSSIONS

### A. Micro-segregations of Solute Elements

The micro-segregation of each solute element during solidification ( $R_c = 1.67 \text{ K/s}$ ) was calculated by Ohnaka and C–K models, respectively, and the calculation results are compared in Figure 7. Since the micro-segregations of Ti and N may be affected by TiN precipitation, their results were temporarily not discussed in this comparison. The results in Figure 7 firstly indicate that Ohnaka and C–K models predicted similar solute segregation ratios. As shown in Table VI, for C and O the micro-segregation ratios calculated by Ohnaka and C–K models were regarded as equivalent. For Si, Mn, P and S, the segregation ratios of these solute elements were also very close in both Ohnaka and C–K model cases. The specific segregation ratios of these four elements at several solidification fractions were compared between the Ohnaka and C–K model cases (see Table VII).

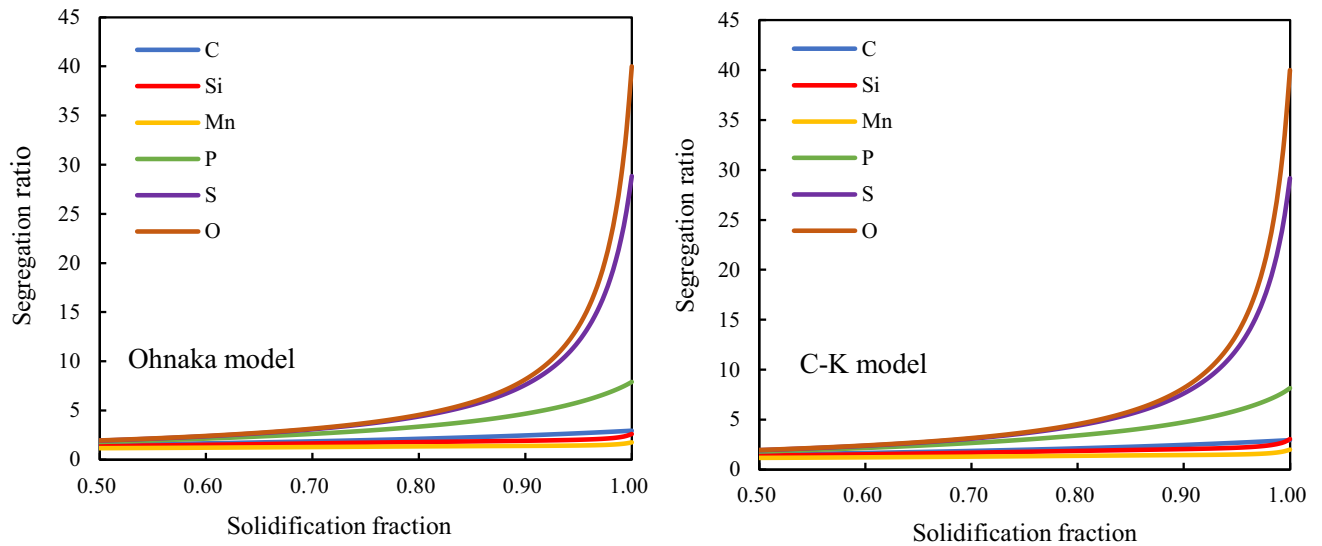


Fig. 7—Comparison of the solute segregation ratios calculated by Ohnaka and C–K models. (Ti, N are not included.)

Second, the sequence of the micro-segregation ratios of these solute elements is  $O > S > P > C > Si > Mn$ . Considering the equilibrium partition coefficient,  $k_i$ , and the diffusion coefficient in solid phase,  $D_i^s$ , of each element (see Table V and Figure 2), this sequence indicates that  $k_i$  probably affects the solute micro-segregation more significantly than  $D_i^s$ . The smaller  $k_i$  is, the larger micro-segregation ratio of element  $i$  would be. The main reason is that the sequence of  $k_i$  is  $O < S < P < C < Si < Mn$ , which perfectly matches the sequence of the reciprocal of solute micro-segregation ratio, while the sequence of  $D_i^s$  does not have a clear correlation with the sequence of solute micro-segregation ratio. For example, although  $D_O^s$  is obviously larger than the values of other elements (see Figure 2), the segregation ratio of oxygen is the highest because  $k_O$  is the lowest among the solute elements.

The segregated solute concentrations calculated by Ohnaka and C–K models, respectively, are shown in Figure 8. It is clearly seen that although the segregation ratio of carbon is in the medium level among the solute elements, the increase in carbon concentration is very obvious because the original carbon concentration in the molten steel is the highest among the solute elements. In comparison, the increases in other solute concentrations are smoother since their original concentrations are relatively lower than carbon's. Based on this result, it is noticeable that for high carbon steel the micro-segregation of carbon would lead to a huge increase in carbon concentration (by about 1.8 wt pct in this study) in the inter-dendrite space during solidification. Therefore, the effect of carbon micro-segregation on the thermodynamic parameters, such as liquidus and solidus temperatures ( $T_l$  and  $T_s$ ) and secondary dendrite arm ( $\lambda$ ), should be seriously considered.

### B. Thermodynamic Calculation of TiN Precipitation

The Ti and N micro-segregation ratios and solute concentrations calculated by Ohnaka and C–K models, respectively, are shown as the solid lines in Figure 9. The dash lines represent for the corresponding imaginary segregation ratios and solute concentrations provided that TiN precipitation is not coupled in the thermodynamic calculations. It is noticeable that if the micro-segregation module is not coupled with the TiN precipitation module, the calculated results would dramatically deviate from the results of the coupled cases. In Figure 9, the turning point refers to the solidification fraction where the TiN precipitation started. As the TiN precipitation proceeded, the micro-segregation of Ti dropped more sharply compared with that of N. This is because that the original concentration of Ti is lower than the value of N by about one order of magnitude. Furthermore, the mass consumption of Ti is more than three times (about 3.43) of the value of N due to TiN precipitation according to stoichiometry.

The curves in Figure 10 show the variations in the liquidus temperature,  $T_l$ , solidus temperature,  $T_s$ , and the solid/liquid interface temperature,  $T_{s-1}$ , of the molten steel with increasing solidification fraction. Due to the micro-segregations of solute elements, the liquidus and solidus temperatures of molten steel decreased obviously instead of keeping as constants. Especially due to the dramatic decrease in  $T_s$ , the temperature range within which the mushy zone of molten steel existed was extended. As a result, the solid/liquid interface temperature, as a function of  $T_l$  and  $T_s$ , dropped to the values near 1200 K.

Figure 11 indicates the precipitation point where the actual activity product of TiN,  $Q_{TiN}$ , became larger than the corresponding equilibrium activity product,  $K'_{TiN}$ . Due to the sharp decrease in  $T_{s-1}$  as shown in Figure 10,

**Table VII. Segregated Ratios of Si, Mn, P and S Calculated by Ohnaka (Left) and C–K (Right) Models**

Solidification Fraction	Si	Mn	P	S
0.2	1.112, 1.113	1.050, 1.050	1.213, 1.214	1.239, 1240
0.5	1.378, 1.385	1.162, 1.163	1.799, 1.807	1.934, 1.935
0.8	1.788, 1.861	1.347, 1.373	3.355, 3.413	4.390, 4.394
0.9	1.920, 2.043	1.398, 1.447	4.671, 4.733	7.612, 7.619
1.0	2.607, 2.849	1.755, 1.991	7.902, 8.151	28.841, 29.169

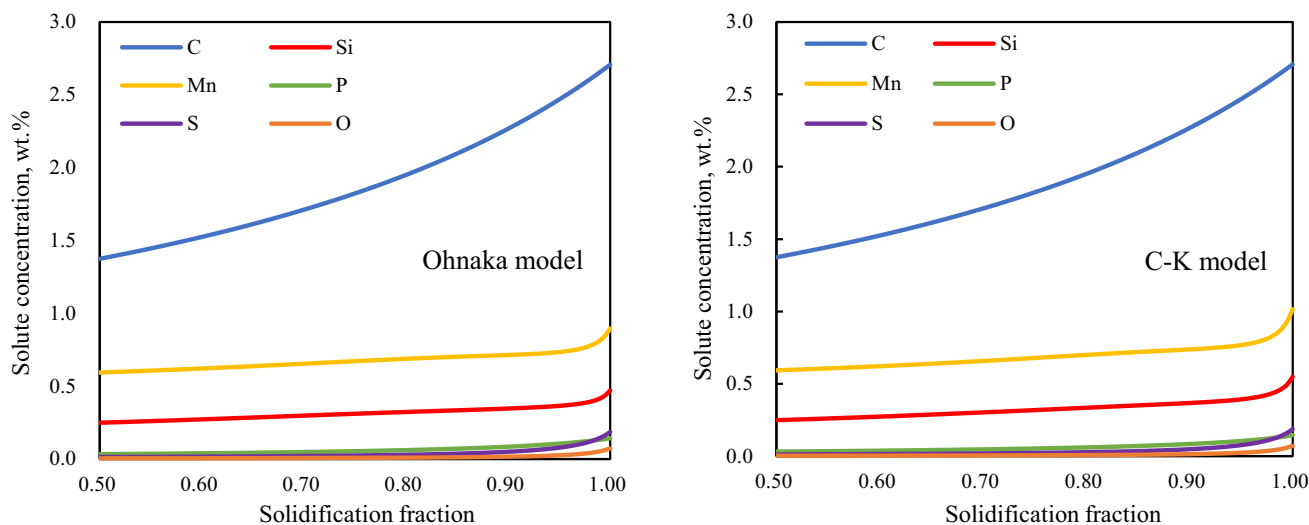


Fig. 8—Comparison of the solute concentrations calculated by Ohnaka and C–K models. (Ti, N are not included.)

$K'_{\text{TiN}}$  as a function of  $T_{s-1}$  also dropped significantly. In the Ohnaka and C–K model cases, the trendlines of  $Q_{\text{TiN}}$  and  $K'_{\text{TiN}}$  intersected at 0.892 and 0.888, respectively ( $R_c = 1.67$  K/s). These two TiN precipitation points were quite close so that the Ohnaka and C–K models could be also treated as equivalent in this thermodynamic calculation. After TiN precipitation,  $Q_{\text{TiN}}$  decreased but kept closely above the value of  $K'_{\text{TiN}}$ . This is because that due to the TiN precipitation,  $\omega_{[\text{Ti}]}$  and  $\omega_{[\text{N}]}$  in one calculation step were re-calculated by Eq. [19] based on  $\omega_{[\text{Ti}]}^e$  and  $\omega_{[\text{N}]}^e$  obtained in its previous step. The difference between  $\omega_{[\text{Ti}]}$  and  $\omega_{[\text{Ti}]}^e$  formed the driving force of the growth of TiN particle.

### C. Kinetic Calculation of TiN Particle Growth

To estimate the radius of growing TiN particle during solidification,  $D_{\text{Ti}}^L$  and  $(\omega_{[\text{Ti}]} - \omega_{[\text{Ti}]}^e)$  as functions of growing time should be first determined as indicated by Eq. [25]. In this section, three molten steel cooling rates, *i.e.*, 1.67, 0.83 and 0.17 K/s, were, respectively, considered in the calculations, aiming to investigate the effect of cooling rate on the TiN inclusion growth behavior.

Based on the thermodynamic calculation data, the variations in  $D_{\text{Ti}}^L$  and  $(\omega_{[\text{Ti}]} - \omega_{[\text{Ti}]}^e)$  with growing time under these three cooling rate conditions are shown in Figure 12. The specific fitting functions for  $D_{\text{Ti}}^L$  and  $(\omega_{[\text{Ti}]} - \omega_{[\text{Ti}]}^e)$  are listed in Table VIII. It is shown that the diffusion coefficient of Ti in the liquid phase,  $D_{\text{Ti}}^L$ , decreased almost linearly due to the decreasing temperature with TiN growing time. The driving force  $(\omega_{[\text{Ti}]} - \omega_{[\text{Ti}]}^e)$  first decreased sharply at the early stage of TiN growth and then the decreasing slope gradually became smoother and finally reached a relatively stable level. This trend was similar to that of  $\omega_{[\text{Ti}]}$  during the TiN precipitation period, as shown in Figure 9. When TiN precipitation started, the segregated Ti concentration in the liquid steel was still relatively high, which made the driving force  $(\omega_{[\text{Ti}]} - \omega_{[\text{Ti}]}^e)$  large and benefited the TiN particle growth. Due to the consumption of Ti concentration,  $\omega_{[\text{Ti}]}$  dropped significantly and this sharply decreased the Ti concentration gradient between the liquid phase and the region near TiN particle. As a result, the TiN growth

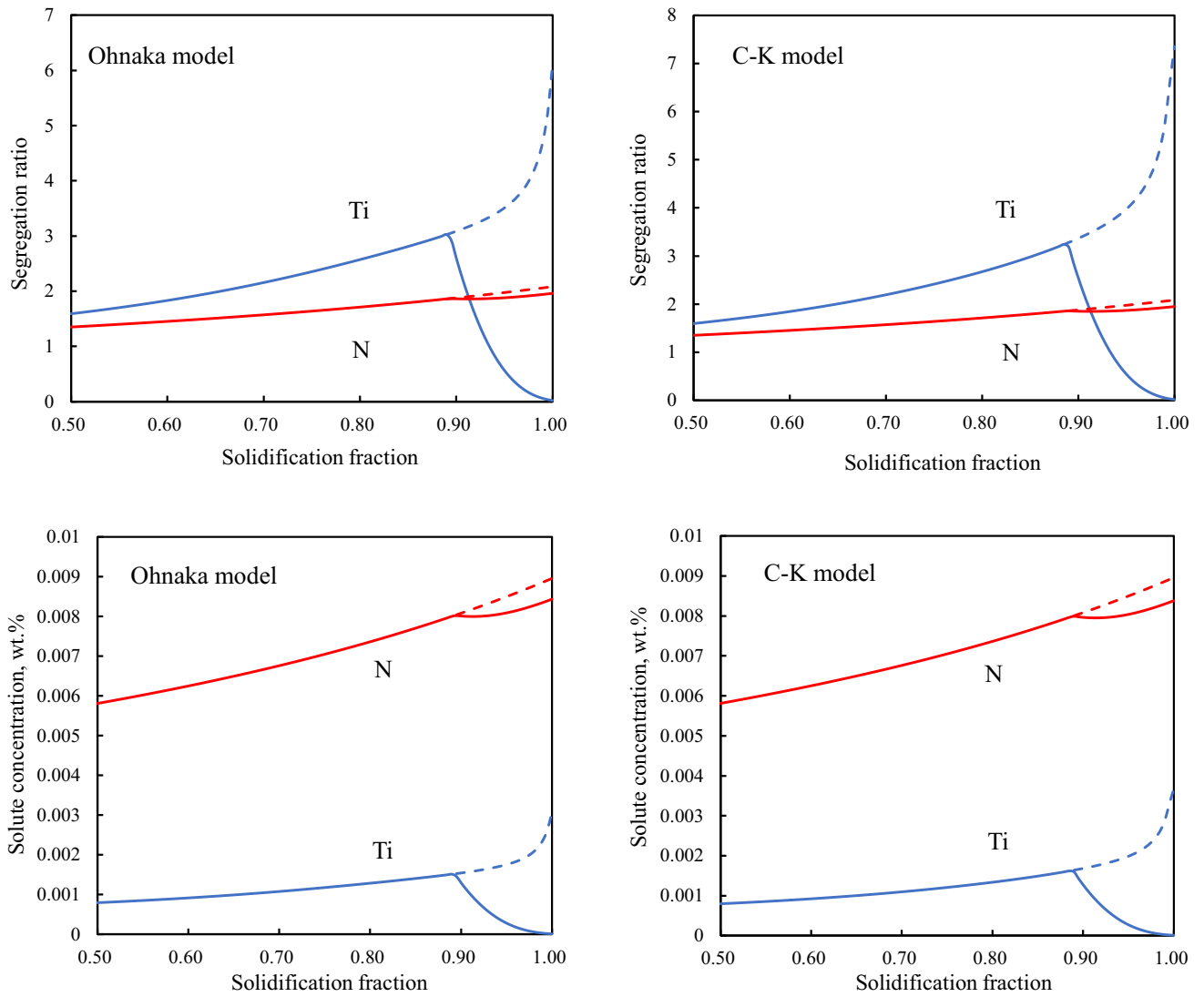


Fig. 9—Ti and N segregation ratios and solute concentrations under the influence of TiN precipitation. Dash lines represent the imaginary counterparts provided that the TiN precipitation is not coupled in the calculation.

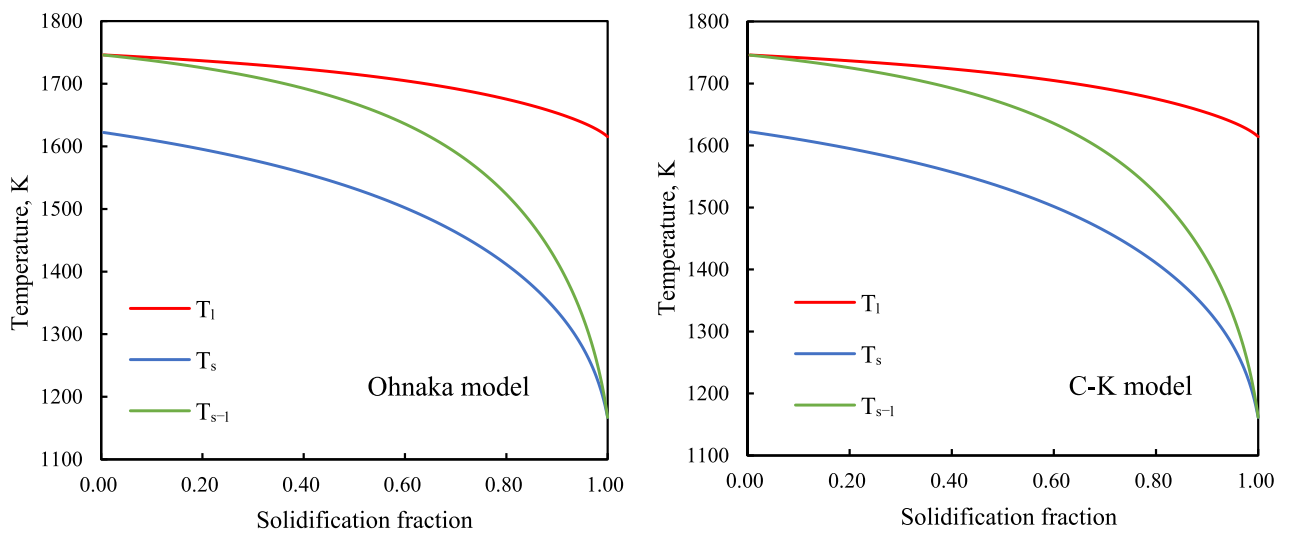


Fig. 10—Variations in  $T_l$ ,  $T_s$ , and  $T_{s-1}$  of molten steel during solidification in Ohnaka and C-K model cases. ( $R_c = 1.67$  K/s).

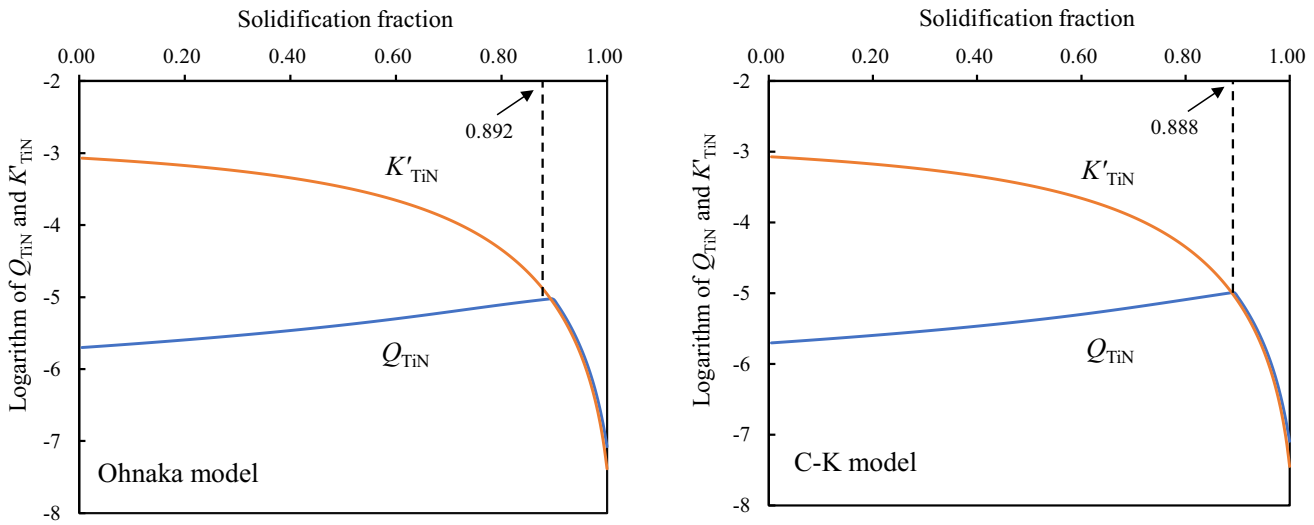


Fig. 11—Variations in  $Q_{\text{TiN}}$  and  $K'_{\text{TiN}}$  during solidification in Ohnaka and C-K model cases. ( $R_c = 1.67$  K/s).

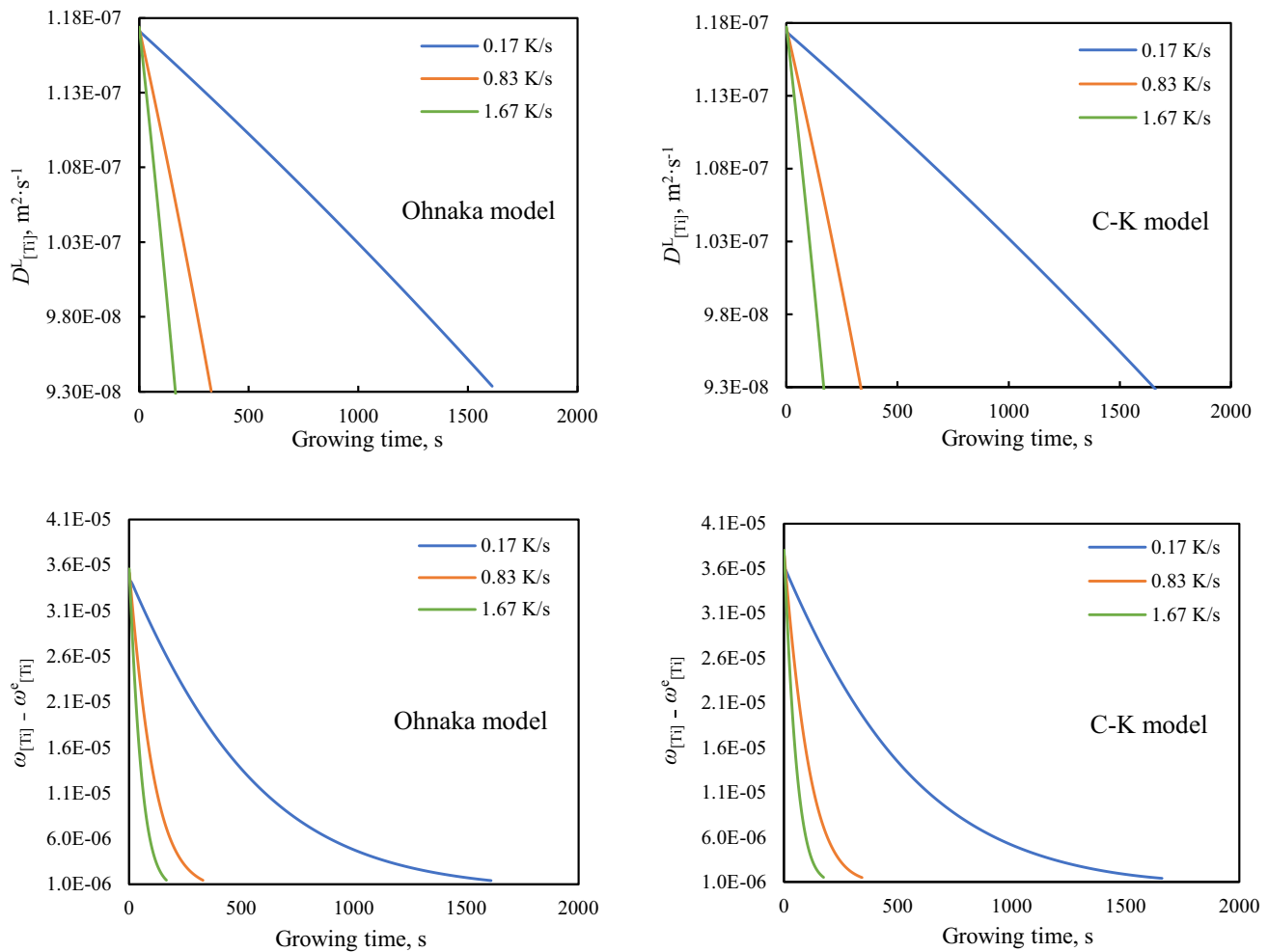


Fig. 12—Variations in  $D_{\text{TiN}}^L$  and  $(\omega_{\text{TiN}} - \omega_{\text{TiN}}^e)$  with increasing growing time under three cooling rate conditions.



gradually became slowly, which in turn limited the consumption of Ti concentration in the liquid phase. Consequently, as TiN growth proceeded, the driving force  $(\omega_{[\text{Ti}]} - \omega_{[\text{Ti}]}^e)$  decreased more smoothly and gradually reached a relative equilibrium state until the steel solidification process finished. By substituting the expressions of  $D_{\text{Ti}}^L$  and  $(\omega_{[\text{Ti}]} - \omega_{[\text{Ti}]}^e)$  into Eq. [25], the variation in TiN particle radius with solidification fraction in each cooling rate case was obtained and the relevant result is shown in Figure 13.

The trendlines of all three cooling rate cases in Figure 13 indicate that as solidification proceeded since TiN precipitation started, the growth curves of TiN particle followed a parabolic relationship with growth time. The particle first grew quickly at the early stage of precipitation and then the growth rate gradually slowed down and finally the particle radius reached a relatively stable value. With  $R_c$  increasing from 0.17 to 0.83 K/s, the solidification fraction at which the precipitation started,  $g_{\text{TiN}}$ , shifted from 0.895 to 0.893 for Ohnaka model case and from 0.892 to 0.889 for C–K model case, respectively. The TiN particle size at the end of solidification,  $d_{g=1}$ , decreased from about 10 to about 4  $\mu\text{m}$ . With  $R_c$  further increasing from 0.83 to 1.67 K/s,  $g_{\text{TiN}}$  shifted from 0.893 to 0.892 for Ohnaka model case and from 0.889 to 0.888 for C–K model case, respectively. The value of  $d_{g=1}$  decreased from about 4 to about 3  $\mu\text{m}$ . The above analysis first indicates that as the cooling rate increased, the TiN precipitation became earlier but the final particle size got smaller. Furthermore, as  $R_c$  increased from 0.83 to 1.67 K/s, the change in  $d_{g=1}$  was less significantly than that as  $R_c$  increased from 0.17 to 0.83 K/s. This illustrates that when  $R_c$  is above a certain value,  $d_g$  would probably be within a narrow range and hence further increasing  $R_c$  may be not a cost-effective way of decreasing TiN inclusion size.

The calculated TiN inclusion radius under different cooling rate conditions were compared with the reference values measured in the metallographic images of TiN inclusions published in the previous studies relating to TiN precipitation in high carbon tire cord steel.<sup>[9,12,38–43]</sup> Some typical images showing the morphologies of TiN inclusions precipitated in SWRH82A tire cord steel were referenced as displayed in Figure 14. Based on these images, it can be seen that the TiN inclusion sizes are not uniform. The larger particle (left) is about 6.0  $\mu\text{m}$  and the smaller ones (right) are about 3.0  $\mu\text{m}$ . Considering that the observed individual TiN particles cannot represent all the TiN inclusions in the steel, a summary of the TiN particle size distribution in the tire cord steels with different carbon contents was also referenced as shown in Table IX. It can be seen that for the tire cord steel with 0.93 wt pct carbon content ( $R_c = 1.5$  K/s), the average size of measured TiN inclusions is 3.32  $\mu\text{m}$  which basically agrees with the calculated size of 3.15  $\mu\text{m}$  (green line:  $R_c = 1.67$  K/s) shown in Figure 13. These TiN inclusion images and statistical data generally validate the kinetic calculations in this

study and this agreement provides a substantial support for the thermodynamic studies of nonmetallic inclusions of steel in the future work.

## V. CONCLUSIONS

A systematic thermodynamic analysis of the precipitation of TiN inclusion during the solidification of SWRH92A high carbon tire cord steel was conducted in this paper. Finite volume method was used in the calculation to mimic the dynamic solute variation in the inter-dendrite space as the solidifying front pushed forward during solidification. In the thermodynamic calculation, the micro-segregations of solute elements and their influence on thermodynamic parameters were particularly taken into account. Ohnaka and Clyne–Kurz models were, respectively, applied to the solute micro-segregation calculations. To consider the influence of TiN precipitation on the micro-segregations of Ti and N, the coupling calculation between TiN precipitation and solute micro-segregation was activated when the condition of TiN precipitation was satisfied. Furthermore, the kinetic calculation of TiN growth was conducted based on the thermodynamic calculation results. The main conclusions are listed as follows:

1. The sequence of the micro-segregation ratios of the solute elements (excluding Ti and N) in the SWRH92A molten steel is  $\text{O} > \text{S} > \text{P} > \text{C} > \text{Si} > \text{Mn}$ . The micro-segregation ratio of each solute element is mainly dependent on its equilibrium partition coefficient between the solid and liquid steel phases,  $k_i$ . The smaller  $k_i$  is, the larger micro-segregation ratio of element  $i$  would be.
2. The concentration of carbon increased most significantly (by about 1.8 wt pct) among the solute elements in the inter-dendrite space during solidification of its highest original content. This result indicates that the effect of carbon micro-segregation on the thermodynamic calculations of high carbon steel products should be seriously considered.
3. By coupling the solute micro-segregation module with the TiN precipitation module, the segregated ratios of Ti and N decreased to different extents after the TiN precipitation, which obviously differed from the trends in the calculation case where the TiN precipitation module was not coupled with the segregation module.
4. When the Ohnaka model and Clyne–Kurz model were, respectively, applied in the thermodynamic calculation, the TiN precipitation point,  $g_{\text{TiN}}$ , was 0.892 and 0.888, respectively. The close values indicate that these two micro-segregation models can be regarded as equivalent in this thermodynamic study.
5. With  $R_c$  increasing from 0.17 to 1.67 K/s,  $g_{\text{TiN}}$  shifted from 0.895 to 0.892 for Ohnaka model case and from 0.892 to 0.888 for Clyne–Kurz model case, respectively. This indicates that TiN precipitation would occur earlier as  $R_c$  increased. However, the TiN

**Table VIII. Fitting Functions for  $D_{Ti}^L$  and  $(\omega_{[Ti]} - \omega_{[Ti]}^e)$  in the Ohnaka and C-K Model Cases**

$R_c$ , K/s	Ohnaka Model Case	C-K Model Case
0.17	$D_{Ti}^L = -1.46 \times 10^{-7}t + 1.174 \times 10^{-3}$	$D_{Ti}^L = -1.46 \times 10^{-7}t + 1.177 \times 10^{-3}$
0.83	$D_{Ti}^L = -7.30 \times 10^{-7}t + 1.176 \times 10^{-3}$	$D_{Ti}^L = -7.30 \times 10^{-7}t + 1.180 \times 10^{-3}$
1.67	$D_{Ti}^L = -1.46 \times 10^{-6}t + 1.177 \times 10^{-3}$	$D_{Ti}^L = -1.46 \times 10^{-6}t + 1.180 \times 10^{-3}$

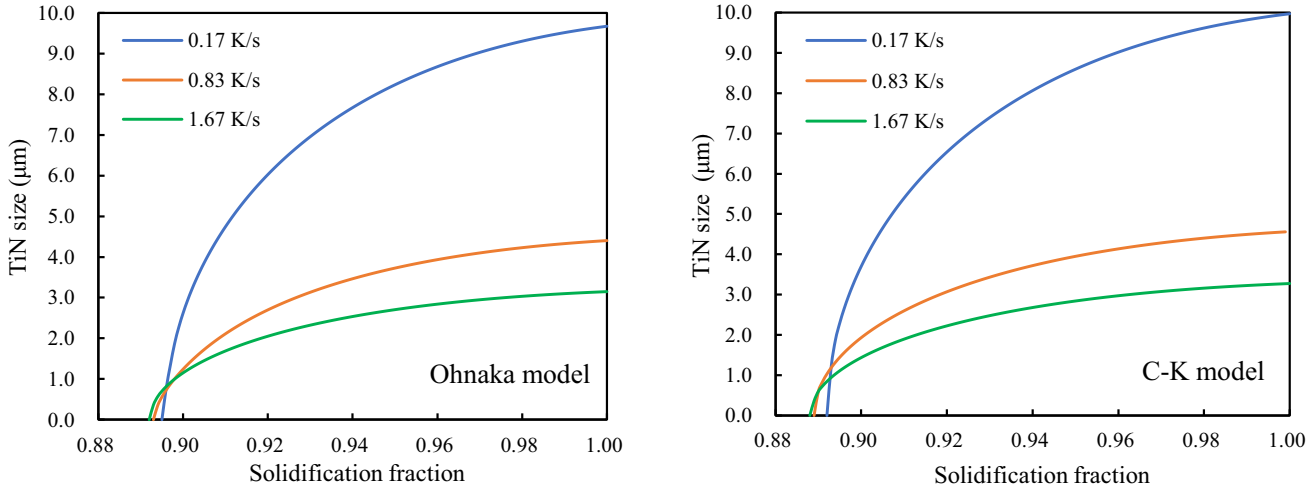


Fig. 13—Variation in TiN particle size with increasing solidification fraction.

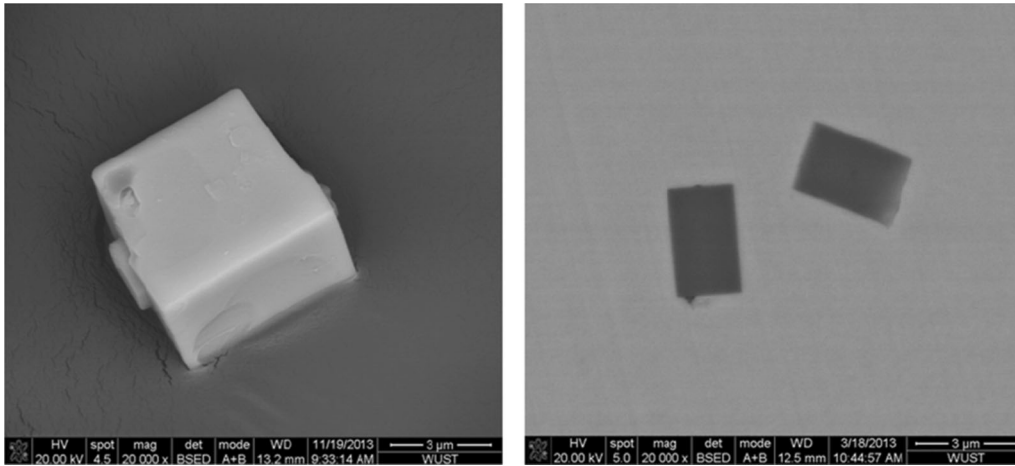


Fig. 14—Morphologies of TiN inclusions observed in the samples of SWRH82A tire cord steel. ( $R_c$  was about 1.5 K/s) Reprinted with permission from Ref. [38].

**Table IX. TiN Particle Size Distribution in the Tire Cord Steels With Different Carbon Contents**

Carbon Content (Wt Pct)	TiN Particle Size Distribution (Pct)			Average Size ( $\mu\text{m}$ )
	0–4 $\mu\text{m}$	4–5 $\mu\text{m}$	> 5 $\mu\text{m}$	
0.71	88.60	10.13	—	2.60
0.80	79.33	14.75	4.92	2.99
0.93	72.61	17.89	9.52	3.32

( $R_c$  was about 1.5 K/s). Reprinted with permission from Ref. [38].

particle size decreased from about 10 to about 3  $\mu\text{m}$  as  $R_c$  increased within this range.

- The calculated TiN inclusion size was well validated by the metallographic images of TiN inclusions and the statistical data of TiN particle size distribution in high carbon tire cord steel published in the previous studies. This agreement encourages the proposed thermodynamic calculation method and sets an example for the future thermodynamic studies of nonmetallic inclusions of steel.

## ACKNOWLEDGMENTS

The authors gratefully acknowledge the financial support for this work from the National Natural Science Foundations of China (Grant Nos. 51874214, 51804230), China Postdoctoral Science Foundation (Grant No. 2020M672425), and Hubei Provincial Natural Science Foundation (Grant No. 2020CFB133).

## REFERENCES

- S.K. Michellic, D. Loder, T. Reip, A. Ardehali Barani, and C. Bernhard: *Mater. Charact.*, 2015, vol. 100, pp. 61–67.
- V. Descotes, S. Migot, F. Robaut, J.P. Bellot, V. Perrin-Guérin, S. Witzke, and A. Jardy: *Metall. Trans. A*, 2015, vol. 46A, pp. 2793–95.
- J.Y. Li and W.Y. Zhang: *ISIJ Int.*, 1989, vol. 29, pp. 158–64.
- J.Y. Yang, C. Ling, J.Z. Tang, C. Ni, and L.C. Xiao: *Heat Treat. Met.*, 2012, vol. 37, pp. 32–37.
- J. Petit and C. Sarrazin-Baudoux: *Key Eng. Mater.*, 2015, vol. 627, pp. 153–56.
- W. Yan, Y.Y. Shan, and K. Yang: *Metall. Trans. A*, 2007, vol. 38A, pp. 1211–22.
- J.L. Lei, Z.L. Xue, and Y.D. Jiang: *Metal. Int.*, 2012, vol. 17, pp. 10–15.
- J.L. Lei, Z.L. Xue, Y.D. Jiang, J. Zhang, R. Xiong, and F. Zou: *J. Mater. Metall.*, 2014, vol. 13, pp. 125–27.
- H.Y. Liu, H.L. Wang, L. Li, J.Q. Zheng, Y.H. Li, and X.Y. Zeng: *Ironmak. Steelmak.*, 2011, vol. 38, pp. 53–58.
- J. Fu, J. Zhu, L. Di, F. Tong, and Y. Wang: *Acta Metall. Sin.*, 2000, vol. 36, pp. 801–804.
- Y.D. Jiang, Z.L. Xue, and J. Zhang: *J. Iron Steel Res. Int.*, 2014, vol. 21 (Supplement 1), pp. 91–94.
- J.L. Lei, D.N. Zhao, Y.J. Fu, and X.F. Xu: *Arch. Foundry Eng.*, 2019, vol. 19, pp. 33–37.
- Z.L. Xue, W.T. Jin, J.L. Lei, and Y.D. Jiang: *Steelmaking*, 2016, vol. 32, pp. 23–32.
- X.F. Cai, Y.P. Bao, M. Wang, L. Lin, N.C. Dai, and C. Gu: *Metall. Res. Tech.*, 2015, vol. 112, pp. 407–18.
- L. Wang, Z.L. Xue, H.Y. Zhu, and J.L. Lei: *Results Phys.*, 2019, vol. 14, pp. 102428–434.
- J. Chen: *Manual of Chart and Data in Common Use of Steel Making*, 2nd ed., The Metallurgical Industry Press, Beijing, 2010, p. 510.
- Q. Tian, G.C. Wang, Y. Zhao, J. Li, and Q. Wang: *Metall. Trans. B*, 2018, vol. 49B, pp. 1149–64.
- Z. Ma and D. Janke: *ISIJ Int.*, 1998, vol. 38, pp. 46–52.
- X. F. Wan, J. S. Meng, D. G. Li, D. Y. Guo, J. X. Jia, X. W. Liao and D. Cao: *Proc. Int. Symp. on Clean Steel Prod. Tech.*, The Chinese Society for Metals, Anshan, 2018, pp. 171–75.
- D.L. You, S.K. Michellic, P. Presoly, J.H. Liu, and C. Bernhard: *Metals*, 2017, vol. 7, p. 460.
- E. Scheil: *Metallkunde*, 1942, vol. 34, pp. 70–72.
- H.D. Brody and M.C. Flemings: *Trans. Metall. Soc. AIME*, 1966, vol. 236, pp. 615–24.
- T.W. Clyne and W. Kurz: *Metall. Trans. A*, 1981, vol. 12A, pp. 965–71.
- I. Ohnaka: *Trans. Iron Steel Inst. Japan*, 1986, vol. 26, pp. 1045–51.
- L. Wang, Z.L. Xue, Y.L. Chen, and X.G. Bi: *Processes*, 2020, vol. 8, pp. 10–22.
- J.L. Lei, D.N. Zhao, H.Y. Zhu, and Y.D. Jiang: *Steelmaking*, 2018, vol. 34, pp. 66–71.
- E.B. Yue, S.T. Qiu, and Y. Gan: *J. Iron Steel Res.*, 2007, vol. 19, pp. 35–38.
- S. Luo, M.Y. Zhu, C. Ji, and Z.Z. Cai: *Iron Steel*, 2010, vol. 45, pp. 31–36.
- L. Yang, G.G. Cheng, S.J. Li, M. Zhao, and G.P. Feng: *ISIJ Int.*, 2015, vol. 55, pp. 1693–98.
- X. Zhang, G.J. Ma, and M.K. Meng: *Philos. Magn.*, 2019, vol. 99, pp. 1041–56.
- Y.M. Won and B.G. Thomas: *Metall. Trans. A*, 2001, vol. 32A, pp. 1755–67.
- Z.Z. Liu, J. Wei, and K.K. Cai: *ISIJ Int.*, 2002, vol. 42, pp. 958–63.
- D.L. Hu, H. Liu, J.B. Xie, J. Cheng, J. Li, and J.X. Fu: *J. Iron Steel Res. Int.*, 2018, vol. 25, pp. 803–12.
- W.J. Ma, Y.P. Bao, L.H. Zhao, and M. Wang: *Metall. Mater.*, 2014, vol. 21, pp. 234–39.
- Y.N. Wang, J. Yang, X.L. Xin, R.Z. Wang, and L.Y. Xu: *Metall. Trans. B*, 2016, vol. 47B, pp. 1378–89.
- J.H. Shin and J.H. Park: *Metall. Trans. B*, 2020, vol. 51B, pp. 1211–24.
- D.L. You, S.K. Michellic, C. Bernhard, D. Loder, and G. Wieser: *ISIJ Int.*, 2016, vol. 56, pp. 1770–78.
- C.F. Yu and Z.L. Xue: *J. Wuhan Uni. Sci. Tech.*, 2015, vol. 38, pp. 241–44.
- Y. H. Li, J. Q. Zheng, G. Q. Lin and H. Y. Liu: *Proc. Symp. on Adv. Spec. Steel Prod. Tech.*, The Chinese Society for Metals, Beijing, 2011, pp. 368–71.
- D. Y. Guo, Y. H. Ren, B. X. Wang, H. Gao and B. Zhang: *Proc. Symp. on Domest. Steelmaking–Continuous Casting Prod. Tech.*, The Chinese Society for Metals, Tangshan, 2014, pp. 327–31.
- H.Y. Liu, J.Q. Zheng, Y.H. Li, G.Q. Lin, Z.L. Xue, and H.L. Wang: *J. Uni. Sci. Tech. Beijing*, 2010, vol. 32, pp. 866–71.
- Z.L. Xue, C.F. Yu, L.W. Qiu, W.T. Chen, and J. Zhang: *J. Chongqing Univ.*, 2015, vol. 38, pp. 93–98.
- N. Li, L. Wang, Z.L. Xue, C.Z. Li, A. Huang, and F.F. Wang: *Results Phys.*, 2020, vol. 16, pp. 102929–2937.

**Publisher's Note** Springer Nature remains neutral with regard to jurisdictional claims in published maps and institutional affiliations.